The Astrophysical Journal Letters, 893:L5 (6pp), 2020 April 10 https://doi.org/10.3847/2041-8213/ab830e

First Embedded Cluster Formation in California Molecular Cloud

Jin-Long Xu[1,2], Ye Xu[3], Peng Jiang[1,2], Ming Zhu[1,2], Xin Guan[1,2], Naiping Yu[1], Guo-Yin Zhang[1], and Deng-Rong Lu[3]
[1] National Astronomical Observatories, Chinese Academy of Sciences, Beijing 100101, People's Republic of China; xujl@bao.ac.cn, pjiang@bao.ac.cn
[2] CAS Key Laboratory of FAST, National Astronomical Observatories, Chinese Academy of Sciences, Beijing 100101, People's Republic of China
[3] Purple Mountain Observatory, Chinese Academy of Sciences, Nanjing 210008, People's Republic of China
Received 2019 October 29; revised 2020 March 19; accepted 2020 March 21; published 2020 April 8

Abstract

We performed a multi-wavelength observation toward the LkHα 101 embedded cluster and its adjacent $85' \times 60'$ region. The LkHα 101 embedded cluster is the first and only significant cluster in the California molecular cloud (CMC). These observations have revealed that the LkHα 101 embedded cluster is located just at the projected intersectional region of two filaments. One filament is the highest-density section of the CMC, the other is a new identified filament with a low-density gas emission. Toward the projected intersection, we find the bridging features connecting the two filaments in velocity, and identify a V-shaped gas structure. These agree with the scenario that the two filaments are colliding with each other. Using the Five-hundred-meter Aperture Spherical radio Telescope, we measured the radio recombination line velocity of the LkHα 101 H II region to be 0.5 km s^{-1}, which is related to the velocity component of the CMC filament. Moreover, there are some young stellar objects (YSOs) distributed outside the intersectional region. We suggest that the cloud–cloud collision, together with the fragmentation of the main filament, may play an important role in the YSOs' formation of the cluster.

Unified Astronomy Thesaurus concepts: Interstellar clouds (834); Star formation (1569); Dynamical evolution (421)

1. Introduction

High-mass stars ($>8\,M_{\odot}$) play an important role in promoting the evolution of their host galaxies (Zinnecker & Yorke 2007). However, how the high-mass stars form is not yet well understood. Most high-mass stars usually form in stellar clusters (Lada & Lada 2003). In order to understand how a high-mass star forms, we must understand the formation of its host embedded cluster. Recently, young embedded cluster-forming systems have been found to be associated often with the hub-like multiple filamentary structure. Hence, the filament-hub accretion can be used to explain the formation of the young embedded cluster (Myers 2009; Kirk et al. 2013). In addition, individual embedded clusters often present small age spreads (Jeffries et al. 2011; Getman et al. 2017), indicating that a whole cluster of stars precipitates the quasi-instantaneous formation (Elmegreen 2000; Tan et al. 2006). This suggests that a significant amount of dense gas needs to be rapidly gathered in the place where the cluster was born. Collisions between molecular clouds and external effects (e.g., H II region and supernovae) can satisfy the condition for rapid gas accumulation (Elmegreen 1998; Inoue & Fukui 2013). These cloud–cloud collisions have been invoked to explain the formation of super star clusters (Furukawa et al. 2009; Fukui et al. 2014, 2016).

The California molecular cloud (CMC) is a filamentary structure that extends over about 10° in the plane of sky (Lada et al. 2009). In the Perseus constellation, the CMC is considered to be the most massive giant molecular cloud in the range of 0.5 kpc from the Sun (Lada et al. 2009). Despite its large size and mass, the CMC appears to be very modest in its star formation activity. In the CMC, the LkHα 101 embedded cluster is the first and only significant cluster, which is consistent with the entire LkHα 101 H II region (Barsony et al. 1990; Dzib et al. 2018). In the embedded cluster, the star LkHα 101 is a young high-mass star with a spectral type of near B0.5 (Herbig et al. 2004; Wolk et al. 2010). Compared to the Orion nebula that contains many OB stars, the CMC is a sleeping giant (Lada et al. 2017). Hence, the CMC provides us with an ideal laboratory for investigating the formation of embedded cluster. In this Letter, we performed a multi-wavelength study to investigate the formation imprint of the LkHα 101 embedded cluster in the CMC.

2. Observation and Data Processing

To show the molecular gas distribution surrounding the LkHα 101 embedded cluster, we mapped a $85' \times 60'$ region centered at the position of the LkHα star in the transitions of ^{12}CO $J = 1$–0, ^{13}CO $J = 1$–0 and C^{18}O $J = 1$–0 lines using the Purple Mountain Observation (PMO) 13.7 m radio telescope, during 2019 May and December. The 3×3 beam array receiver system in single-sideband mode was used as the front end. The back end is a fast Fourier transform spectrometer of 16,384 channels with a bandwidth of 1 GHz, corresponding to a velocity resolution of 0.16 km s^{-1} for ^{12}CO $J = 1$–0, and 0.17 km s^{-1} for ^{13}CO $J = 1$–0 and C^{18}O $J = 1$–0. ^{12}CO $J = 1$–0 was observed at the upper sideband with a system noise temperature (Tsys) of ∼280 K, while ^{13}CO $J = 1$–0 and C^{18}O $J = 1$–0 were observed simultaneously at the lower sideband with a system noise temperature of ∼150 K. The half-power beamwidth (HPBW) was 53″ at 115 GHz. The pointing accuracy of the telescope was better than 5″. Mapping observations used the on-the-fly mode with a constant integration time of 14 s at each point and with a $0.'5 \times 0.'5$ grid. The reference-point position was at $l = 165.^{\circ}2993$ and $b = -9.^{\circ}2197$. The standard chopper-wheel method was used to calibrate the antenna temperature (Ulich & Haas 1976). The calibration errors were estimated to be within 10%.

Moreover, we observed the LkHα 101 H II region associated with the LkHα 101 embedded cluster in the C168α (1375.28630 MHz) and H168α (1374.60043 MHz) radio recombination lines (RRLs) using the Five-hundred-meter Aperture Spherical radio Telescope (FAST), during 2019

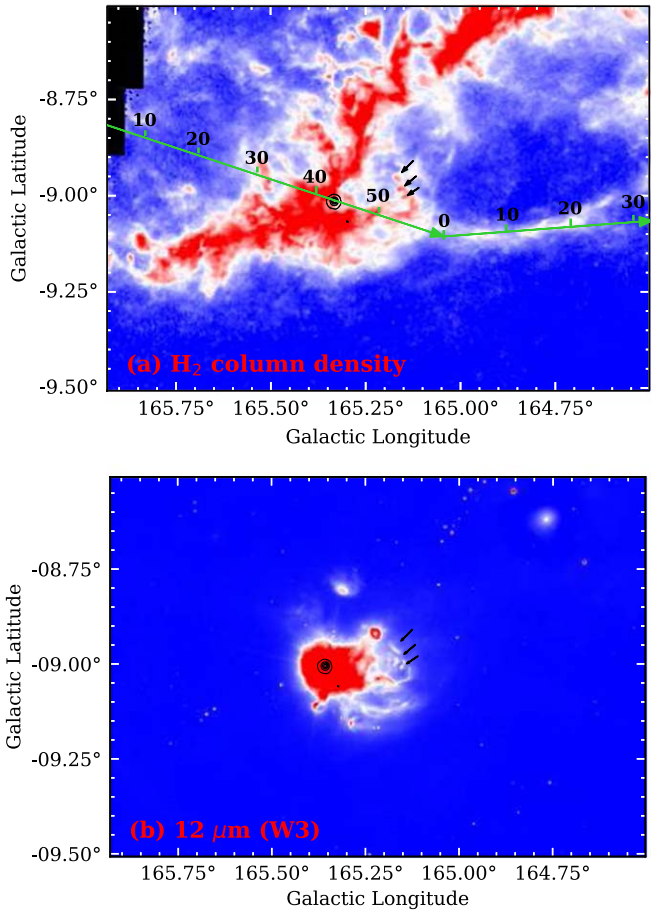

Figure 1. 1.4 GHz radio continuum contours in black, overlaid on the Herschel H_2 column density and WISE 12 μm images of the observed region in (a) and (b) panels, respectively. The black contours begin at 5σ in steps of 10σ, with $1\sigma = 0.7$ mJy beam^{-1}. The black arrows mark the positions of several pillars. The two green arrows mark the direction and position of position–velocity diagram in Figure 3. We also label the offsets (y-axis in Figure 3) over the two arrows.

September. FAST is located in Guizhou, China. The aperture of the telescope is 500 m and the effective aperture is about 300 m. The HPBW was 2.′9 and the velocity resolution is 0.1 km s^{-1} for the digital back end at 1.4 GHz. Single-pointing observation of the LkHα 101 H II region was taken with the narrow mode of spectral backend. This mode has 65,536 channels in 31.25 MHz bandwidth. During observations, system temperature was around 18 K. The observed position was integrated for 60 minutes. Reduced root mean square (rms) of the final spectrum was about 11.0 mK. Jiang et al. (2019) gave more details of the FAST instrumentation.

To trace the ionized-gas distribution of the LkHα 101 H II region, we also used the 1.4 GHz radio continuum emission data, obtained from the NRAO VLA Sky Survey with a noise of about 0.45 mJy beam^{-1} and a resolution of 45″ (Condon et al. 1998). In order to trace the polycyclic aromatic hydrocarbon (PAH) emission, we also utilized the 12 μm (W3) infrared data from the survey of the Wide-field Infrared Survey Explorer (WISE; Wright et al. 2010). The infrared band 12 μm has the angular resolutions of 6.″5.

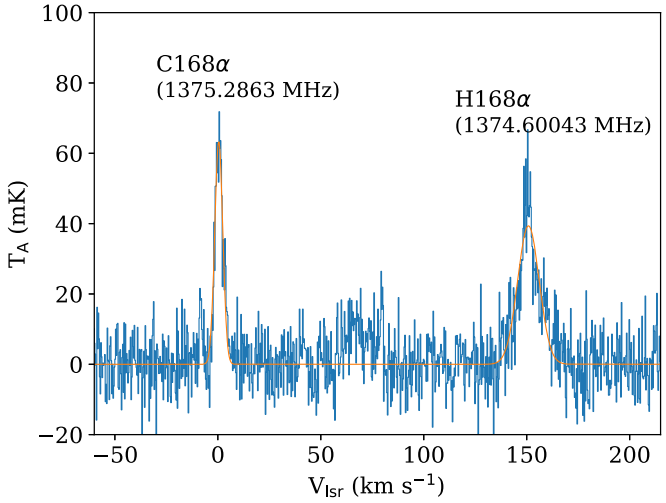

Figure 2. C168α and H168α RRLs spectra of the LkHα 101 H II region from the FAST observations. The red smooth curves are a double-Gaussian fit to the observed spectra. The velocity resolution is smoothed to 0.2 km s^{-1}, then the noise rms is 7.8 mk.

3. Results

3.1. Infrared and Radio Continuum Images

Figure 1(a) shows an H_2 column density map for our observed region. Zhang et al. (2019) constructed the H_2 column density map with a resolution of 18.″2 by using the Herschel data toward the entire CMC. Here, we only cut out a 85′ × 60′ region centered at position of the LkHα 101 star from the H_2 column density map. In Figure 1(a), the H_2 column density map shows a filamentary structure elongated from southeast to northwest, named main filament. The main filament is consistent with a filamentary dark cloud L1482 (Harvey et al. 2013; Li et al. 2014), which is the highest-density part of the CMC (Lada et al. 2017; Zhang et al. 2019). As marked by the two green long arrows in Figure 1(a), we identify a new filament with a low-density gas emission, named minor filament. The minor filament appear to be perpendicular with the main filament in the line of sight.

The 1.4 GHz radio continuum emission can be used to trace ionized gas. In Figure 1(a), the ionized-gas emission in the black contours of the LkHα 101 H II region has a compact structure, which is located at the intersectional region of the main and minor filaments. The WISE 12 μm contains PAH emission (Tielens 2008). The PAH molecules are excited by the ultraviolet (UV) radiation from the H II region. In Figure 1(b), the PAH emission shows a bubble-like structure and several pillars, indicating that the expanding bubble created by the LkHα 101 H II region is interacting with the main filament. Figure 2 shows the C168α and H168α RRLs spectra of the LkHα 101 H II region from the FAST observations. We use the double-Gaussians to fit the data. Compared to the H168α RRL, the C168α RRL with a narrow line width is more suitable for tracing the RRL velocity of ionized gas. Hence, we obtain the RRL velocity of 0.5 ± 0.1 km s^{-1} for the LkHα 101 H II region.

3.2. Molecular Gas Images

H_2 column density only gives the distribution of projected 2D gas. Here, we use ^{12}CO $J = 1$–0, ^{13}CO $J = 1$–0, and C^{18}O $J = 1$–0 lines to trace the molecular gas distribution of the two

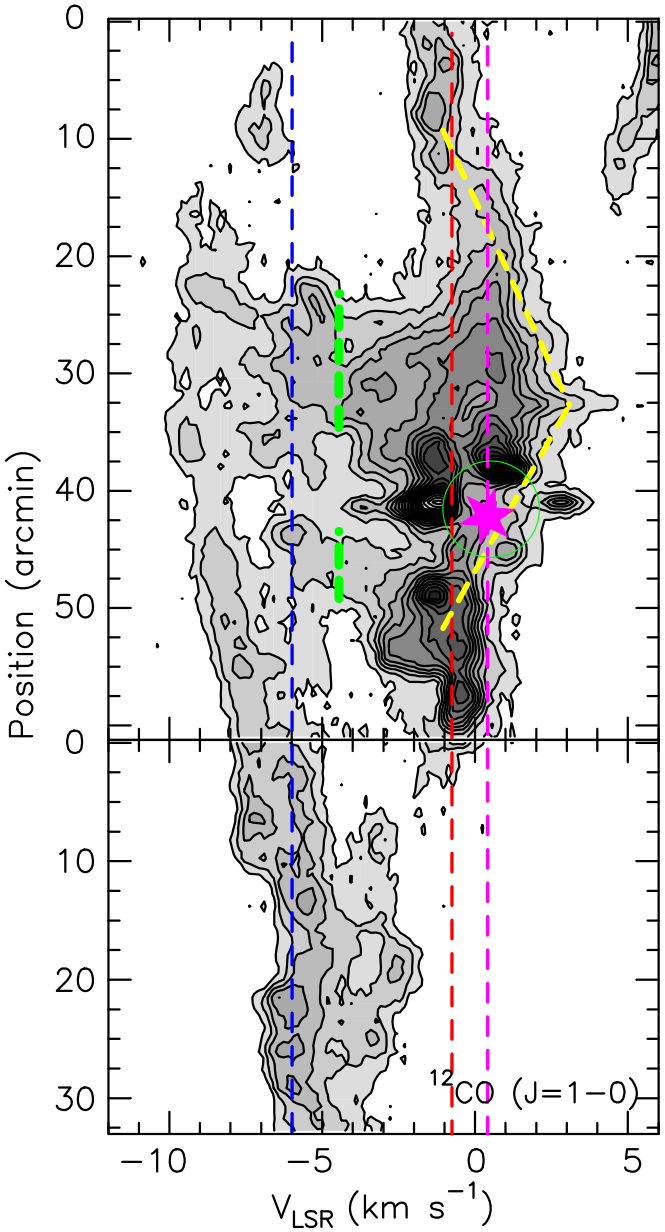

Figure 3. PV diagram of the ^{12}CO $J = 1$–0 emission along the minor filament, as shown by the black dashed line in Figure 1(a). The red dashed line marks the systemic velocity of -0.7 km s^{-1} for the main filament. The purple dashed line indicates the RRL velocity of 0.5 km s^{-1} for the LkHα 101 H II region. The blue dashed line indicates the systemic velocity of -6.0 km s^{-1} for the minor filament. The contour levels are 10, 20, …, 90% of the peak value. The bridging positions are indicated by green dashed lines. The purple star represents the LkHα 101 H II region or LkHα 101 embedded cluster. The green circle indicates a molecular shell. A V-shaped gas structure is indicated by the yellow dashed lines.

filaments. To investigate the gas structure of the minor filament, we made a position–velocity (PV) diagram (Figure 3) of the ^{12}CO $J = 1$–0 emission along the black dashed line and through the position of the LkHα star in Figure 1. In Figure 3, we see that there are two main velocity components, which range from -10.1 to -4.0 km s^{-1}, and from -4.0 to 4.1 km s^{-1}. In ^{12}CO $J = 1$–0 emission, we can clearly see bridging features in velocity between the two components, indicated by the green dashed lines in Figure 3. Moreover, the ^{12}CO $J = 1$–0 emission shows a molecular shell and a V-shaped gas structure, which are indicated by the green circle and yellow dashed lines, respectively, in Figure 3. Using the two velocity ranges, we make the integrated-intensity maps of ^{12}CO $J = 1$–0, ^{13}CO $J = 1$–0, and C^{18}O $J = 1$–0, overlaid with the 1.4 GHz radio continuum contours (pink) and WISE 12 μm contours (green), as shown in Figures 4(a) and (b). In Figure 4(a), the velocity component of -4.0 to 4.1 km s^{-1} displays a filamentary structure elongated from southeast to northwest, which should belong to the main filament. For the main filament, the ^{12}CO $J = 1$–0 and ^{13}CO $J = 1$–0 emission also show a shell-like structure, just surrounding the LkHα 101 H II region. From the PV diagram, we also see the molecular shell. Compared with the ^{12}CO $J = 1$–0 and ^{13}CO $J = 1$–0 emission, the C^{18}O $J = 1$–0 emission may trace the dense part of the main filament. The C^{18}O $J = 1$–0 emission is likely to be cut into two parts at the position of the LkHα 101 H II region. In Figure 4(b), the velocity component of -10.1 to -4.0 km s^{-1} shows a northeast–southwest filament, whose direction is almost perpendicular to the main filament. Compared with Figure 1(a), the northeast–southwest filament is associated with the minor filament. We did not detect the C^{18}O $J = 1$–0 emission in the whole minor filament, suggesting that the minor filament is not a filament like the main filament with dense gas.

Figures 4(c) and (d) give the spectra in the typical positions of the two filaments. From the C^{18}O $J = 1$–0 spectrum, we learn that the systemic velocity of the main filament is -0.7 km s^{-1}. Because we do not detect the C^{18}O $J = 1$–0 emission in the minor filament, the systemic velocity of -6.0 km s^{-1} for the minor filament is determined by the ^{13}CO $J = 1$–0 emission. The systemic velocities of the two filaments are marked by the blue and red dashed lines in Figure 3, suggesting that although the two filaments intersect each other, the intersection is characterized by two different velocity components. The LkHα 101 embedded cluster within the H II region is just located at the projected intersectional region of the two filaments in the line of sight.

3.3. Young Stellar Object Distribution

Based on two young stellar object (YSO) catalogs, Lada et al. (2017) summarized a new YSO table, which contains 43 Class I YSOs, 116 Class II YSOs, and seven Class III YSOs in the whole CMC. Class I YSOs are protostars with circumstellar envelopes and a timescale of the order of $\sim 10^5$ yr, while Class II YSOs are disk-dominated objects with a $\sim 10^6$ yr (André & Montmerle 1994). The Class III YSOs are the pre-main-sequence stars. In the table there are 18 Class I YSOs, 72 Class II YSOs, and four Class III YSOs in our observed region. Figure 5(a) shows the spatial distribution of these YSOs. To investigate the positional relation of YSOs with the main and minor filaments, we overlaid the selected YSOs on the ^{13}CO $J = 1$–0 emission map (green) of the main filament, and the ^{12}CO $J = 1$–0 emission map (blue) of the minor filament. Class I and Class II YSO sources in Figure 5(a) are found to be mainly distributed along the main filament. The main filament contains $\sim$42% of Class I YSOs and $\sim$62% of Class II YSOs in the CMC while occupying only a small fraction of the total cloud area. The main filament includes most young stars, probably because it is the densest part of the CMC, and has a high gas density. In Figure 5(a), we can also clearly see that, compared with other region in the main filament, the projected intersectional region of the two filaments gathers more Class II YSOs with about 1 Myr.

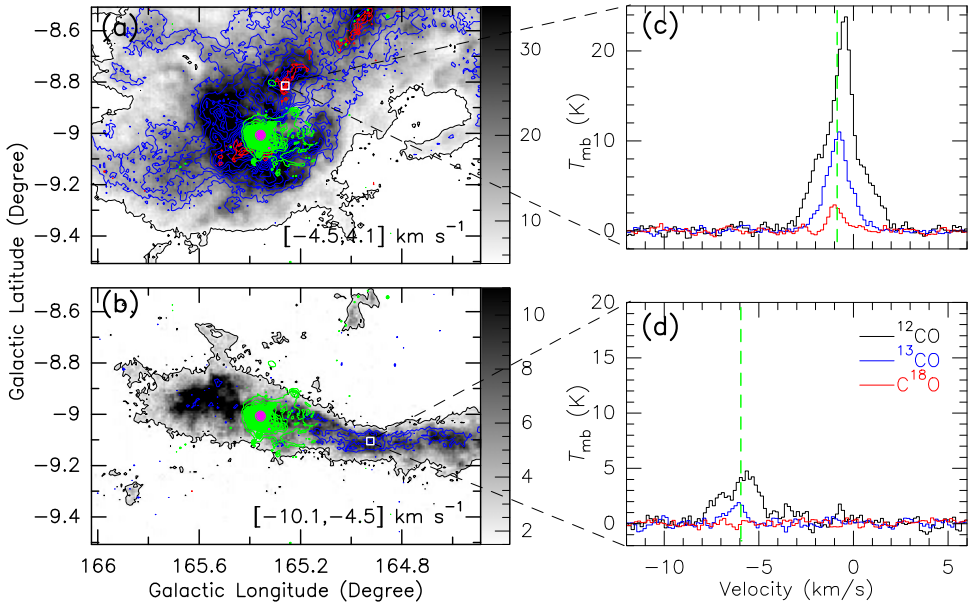

Figure 4. Panels (a) and (b): 1.4 GHz radio continuum contours (pink), WISE 12 μm contours (green), ^{13}CO $J = 1$–0 integrated-intensity contours (blue), and C^{18}O $J = 1$–0 contours (red) superimposed on the integrated-intensity ^{12}CO $J = 1$–0 maps (gray). The integrated velocity ranges are indicated in the lower-right corner of each map. The right gray bar is units of K km s^{-1}. The contours begin at 5σ in each emission. Panels (c) and (d): the typical spectra of the positions are indicated by the white squares in Figures 4(a) and (b).

4. Discussion

4.1. Dynamics Structure

Using the Herschel H_2 column density and CO emission maps, we found the two filaments intersect each other in the line of sight. As shown in the Figure 3, the main and minor filaments have different systemic velocities. It suggests that the intersection from the two filaments is characterized by two different velocity components. This scenario indicates that the two filaments are likely to be colliding with each other. We also find several pieces of evidence to support the colliding idea. In the ^{12}CO $J = 1$–0 PV map, the bridging features connect the two filaments in velocity, which indicates that the two filaments are interacting (e.g., Haworth et al. 2015; Torii et al. 2017; Fukui et al. 2018). In addition, the main filament shows a V-shaped gas structure in the PV diagram, which is similar to that shown in Figure 14 of Fukui et al. (2018). Fukui et al. (2018) suggested that the V-shaped protrusion, including the bridge in a PV diagram, provide a characteristic feature of collision, especially considering that one of the colliding clouds is smaller than the other. We also know that the size of the minor filament is significantly smaller than that of the main filament. For the main filament, the ^{12}CO $J = 1$–0 and ^{13}CO $J = 1$–0 emission present a shell-like structure, which surrounds a PAH bubble created by the LkHα 101 H II region. The shell-like structure detected indicates that the expanding PAH bubble created by the LkHα 101 H II region is interacting with the main filament. However, from Figure 3, we see that the LkHα 101 H II region is still confined to a molecular shell, which is shown in a green circle. Furthermore, the two bridging features in Figure 3 are not connected to the LkHα 101 H II region, indicating that the bridging and V-shaped features are not created by the feedback of the LkHα 101 H II region. Hence, we further conclude that the main filament is colliding with the minor filament.

4.2. The LkHα 101 Embedded Cluster Formation

In the CMC, or main filament, the LkHα 101 embedded cluster with an H II region and several B0.5 stars is the first and only significant cluster (Barsony et al. 1990; Dzib et al. 2018). We see that the LkHα 101 embedded cluster is located just at the projected intersectional position of the main filament with the minor filament. This morphology can be alternatively explained by the filament-hub accretion from the surrounding filament material, which was believed to play an important role in the formation of the young embedded cluster (Myers 2009; Kirk et al. 2013); however, this does not seem to be the case for the LkHα 101 embedded cluster formation in the main filament. We can adopt the RRL velocity (0.5 ± 0.1 km s^{-1}) of the LkHα 101 H II region as the system velocity of the LkHα 101 embedded cluster, which is not located between -10.1 and -4.0 km s^{-1} for velocity component of the minor filament. Hence, the LkHα 101 embedded cluster has no direct contact with the minor filament, and it is impossible for the minor filament to provide material for the embedded cluster formation. Li et al. (2014) proposed that the formation of the embedded cluster was caused by the merging of the two sub-filaments in the main filament. It is very similar to the hub-system accretion model. Furthermore, if there is an accretion flow in the minor filament, such accreting flows will display self-absorption in optically thick emission (Kirk et al. 2013; Lee et al. 2013); this is not found in our ^{12}CO $J = 1$–0 and ^{13}CO $J = 1$–0 data in the main and minor filament, as shown in the Figures 4(c) and (d), respectively.

In addition, the cross-like structure combined by the main and minor filaments seem to be similar to L1188. Gong et al. (2014) suggested that cloud–cloud collision happened in the L1188, and triggered star formation in it. From Section 4.1, we know that the cloud–cloud collision happened in the main filament. The age of the LkHα 101 embedded cluster would be 1–2 Myr (Herbig et al. 2004), suggesting that the LkHα 101 embedded cluster appears to be an individual embedded

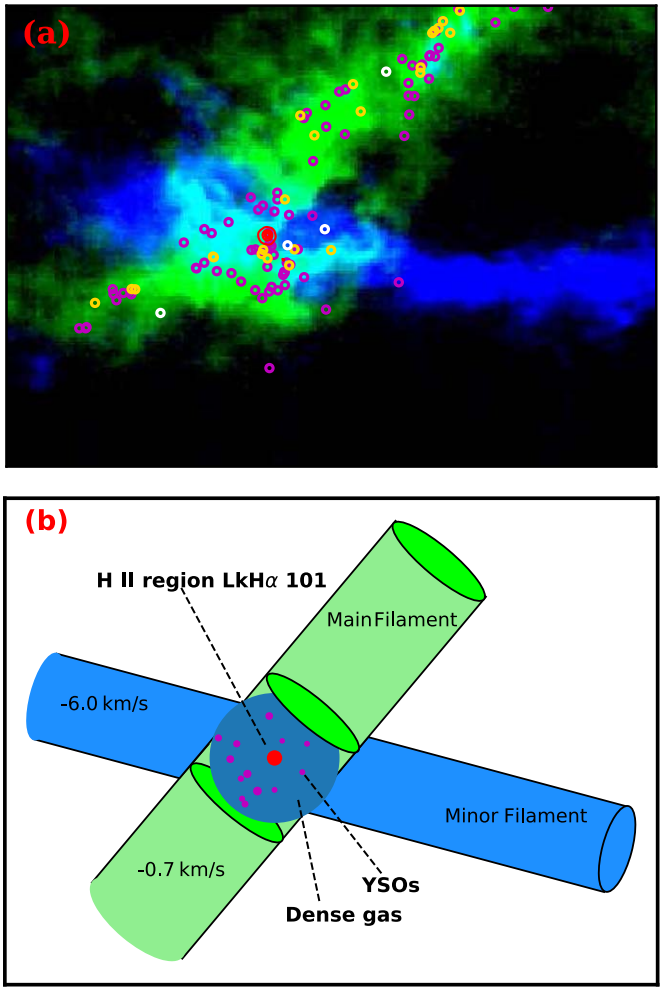

Figure 5. Panel (a): 1.4 GHz radio continuum contours (red) overlaid on the ^{13}CO $J = 1$–0 emission map (green) of the main filament, and ^{12}CO $J = 1$–0 emission map (blue) of the minor filament. The pink circles indicate the positions of Class II YSOs, and the yellow and white circles for Class I YSOs and Class III YSOs, respectively. Panel (b): sketched diagram of the main and minor filaments.

cluster. This suggests that a significant amount of dense gas needs to be rapidly gathered in the position of the main filament where the LkHα 101 embedded cluster was born. Recent magnetohydrodynamic (MHD) numerical simulations of cloud–cloud collision show that after the collision the local density rapidly increases from 300–1000 cm^{-3} to 10^4 cm^{-3} (Inoue & Fukui 2013), suggesting that the cloud–cloud collision can provide help for an embedded cluster formation. Hence, we conclude that the collision between the main and minor filaments may play a certain role in the LkHα 101 embedded cluster formation.

The system velocity of the LkHα 101 embedded cluster is just located between -4.0 and 4.1 km s^{-1} for the velocity component of the main filament, indicating that the LkHα 101 embedded cluster formed in the main filament. The formation circumstances of the LkHα 101 embedded cluster in the CMC is very similar to that of super star cluster RCW 38 (Fukui et al. 2016). The triggered clusters form in the main component, not in the interaction region of two molecular clouds. Figure 5(b) shows a summary for the formation scenario of the LkHα 101 embedded cluster. A super star cluster formation is triggered where two clouds collide at a velocity separation of 10–30 km s^{-1} (Fukui et al. 2016). For the main and minor filaments, the velocity separation is 5.3 km s^{-1}. Therefore, here cloud–cloud collision triggered the formation of the LkHα 101 embedded cluster with B stars, not a super star cluster.

In Figure 5(a), there are some YSOs distributed outside the intersectional region in the main filament. The filament can be fragmented to form prestellar cores and protostars (André et al. 2010). Therefore, the evolution and fragmentation of the main filament may also play an important role in some YSO formation of the LkHα 101 embedded cluster. However, these YSOs do not seem to form a real cluster, suggesting that except for the intersectional region, the other regions seem to have no conditions to produce an embedded cluster in the main filament. Hence, we suggest that the cloud–cloud collision, together with the fragmentation of the main filament, help the LkHα 101 embedded cluster formation in the CMC. Although the present observations can explain the formation of the LkHα 101 embedded cluster, more observations at higher spatial resolution are needed to resolve the detailed kinematics in this region.

5. Conclusions

In this Letter, we present a multi-wavelength observation toward LkHα 101 embedded cluster and its adjacent region. These observations have revealed that the embedded cluster are located just at the projected intersectional region of the main and minor filaments. The main filament is the highest-density part of the CMC, while the minor filament is a new identified filament with a low-density gas emission. In the ^{12}CO $J = 1$–0 PV map, the intersection shows the bridging features connecting the two filaments in velocity, and we also identify a V-shaped gas structure. These agree with the scenario that the two filaments are colliding with each other. From the FAST observation, we obtained the RRL velocity of 0.5 ± 0.1 km s^{-1} for the LkHα 101 H II region, which is located just between -4.5 and 4.1 km s^{-1} for the velocity component of the main filament. We suggest that the collision between the two filaments may play a certain role the LkHα 101 embedded cluster formation in the CMC. In addition, there are also some YSOs distributed outside the intersectional region; this indicates that the evolution and fragmentation of the main filament may also play an important role in the YSO formation of the cluster.

We thank the referee for insightful comments that improved the clarity of this manuscript. This work was supported by the Youth Innovation Promotion Association of CAS, the National Natural Science Foundation of China (grant Nos. 11873019 and 11933011), and also supported by the Open Project Program of the Key Laboratory of FAST, NAOC, Chinese Academy of Sciences.

References

André, P., Men'shchikov, A., Bontemps, S., et al. 2010, A&A, 508, L102
André, P., & Montmerle, T. 1994, ApJ, 420, 837
Barsony, M., Scoville, N. Z., Schombert, J. M., & Claussen, M. J. 1990, ApJ, 362, 674
Condon, J. J., Cotton, W. D., Greisen, E. W., et al. 1998, AJ, 115, 1693
Dzib, S. A., Ortiz-León, G. N., Loinard, L., et al. 2018, ApJ, 853, 99
Elmegreen, B. G. 1998, in ASP Conf. Ser. 148, Origins, ed. C. E. Woodward, J. M. Shull, & H. A. Thronson, Jr. (San Francisco, CA: ASP), 150
Elmegreen, B. G. 2000, ApJ, 530, 277
Elmegreen, B. G., & Lada, C. J. 1977, ApJ, 214, 725

Fukui, Y., Ohama, A., Hanaoka, N., et al. 2014, ApJ, 780, 36
Fukui, Y., Torii, K., Hattori, Y., et al. 2018, ApJ, 859, 166
Fukui, Y., Torii, K., Ohama, A., et al. 2016, ApJ, 820, 26
Furukawa, N., Dawson, J. R., Ohama, A., et al. 2009, ApJL, 696, L115
Getman, K. V., Feigelson, E. D., Kuhn, M.A., et al. 2017, ApJL, 835, L14
Gong, Y., Fang, M., Mao, R., et al. 2014, ApJ, 787, 108
Harvey, P. M., Fallscheer, C., Ginsburg, A., et al. 2013, ApJ, 764, 133
Haworth, T. J., Tasker, E. J., Fukui, Y., et al. 2015, MNRAS, 450, 10
Herbig, G. H., Andrews, S. M., Dahm, S. E., et al. 2004, ApJ, 128, 1233
Inoue, T., & Fukui, Y. 2013, ApJL, 774, L31
Jeffries, R. D., Littlefair, S. P., Naylor, T., & Mayne, N. J. 2011, MNRAS, 418, 1948
Jiang, P., Yue, Y. L., Gan, H. Q., et al. 2019, SCPMA, 62, 959502
Kirk, H., Myers, P. C., Bourke, T. L., et al. 2013, ApJ, 766, 115
Lada, C. J., & Lada, E. A. 2003, ARA&A, 41, 57
Lada, C. J., Lewis, J. A., Lombardi, M., & Alves, J. 2017, A&A, 606, A100
Lada, C. J., Lombardi, M., & Alves, J. F. 2009, ApJ, 703, 52
Lee, K., Looney, L. W., Schnee, S., & Li, Z.-Y. 2013, ApJ, 772, 100
Li, D. L., Esimbek, J., Zhou, J. J., et al. 2014, A&A, 567, A10
Myers, P. C. 2009, ApJ, 700, 1609
Tan, J. C., Krumholz, M. R., & McKee, C. F. 2006, ApJL, 641, L121
Tielens, A. G. G. M. 2008, ARA&A, 46, 289
Torii, K., Hattori, Y., Hasegawa, K., et al. 2017, ApJ, 835, 142
Ulich, B. L., & Haas, R. W. 1976, ApJS, 30, 247
Wolk, S. J., Winston, E., Bourke, T. L., et al. 2010, ApJ, 715, 671
Wright, E. L., Eisenhardt, P. R. M., Mainzer, A. K., et al. 2010, AJ, 140, 1868
Zhang, G.-Y., Xu, J.-L., Vasyunin, A. I., et al. 2019, A&A, 620, A163
Zinnecker, H., & Yorke, H. W. 2007, ARA&A, 45, 481